www.czasopisma.pan.pl PAN www.journals.pan.pl

ARCHIVES of FOUNDRY ENGINEERING

ISSN (2299-2944)
Volume 2025
Issue 1/2025

91 – 102

10.24425/afe.2025.153778

11/1

Published quarterly as the organ of the Foundry Commission of the Polish Academy of Sciences

3D Phase-field Simulations of Spheroidal Cast Irons and Evaluation of Homogenized Elastic Mechanical Properties

R. Nellissery Rajan *, J. Eiken
Access e.V, Germany
* Corresponding author: E-mail address: r.nellissery@access-technology.de

Received 30.07.2024; accepted in revised form 27.11.2024; available online 17.03.2025

Abstract

The Volumetric Multicomponent Multiphase Field model implemented in MICRESS® enables microstructure simulation of spheroidal graphite cast iron in 3D space. In this work, it is combined with the homogenization tool HOMAT to study the correlation between graphite characteristics and effective elastic mechanical properties. In a first step, the microstructure evolution of near-eutectic Fe-C-Si-(Mg) grades is simulated from the pure melt to the as-cast structure. The required thermodynamic and diffusion data are evaluated by run-time coupling to CALPHAD data. Temperature evolution is simulated by balancing latent heat release and heat extraction, considering the casting modulus and the mould diffusivity. During the initial solidification, dendritic austenite and spheroidal graphite nucleate and grow independently in the melt. After encapsulation by austenite, the graphite nodules continue to grow by interstitial diffusion of carbon. The eutectoid decomposition of primary austenite to ferrite and graphite is modelled under assumption of para-equilibrium conditions. The final as-cast structure is characterized by graphite nodules of varying size and morphology distributed in a polycrystalline, fully ferritic matrix. To generate representative volume elements (RVE) with different characteristics of graphite precipitates, a series of simulations are performed under independent variation of chemical composition, casting modulus and nucleation conditions. From each RVE, the graphite fraction, the nodule number, the mean nodule size and the mean sphericity are evaluated. In a second step, the RVEs are transferred to the HOMAT software and homogenized values for the Young's modulus, the shear modulus, and the Poisson's ratio are evaluated and discussed in correlation with the characteristic graphite properties and classic mean field approaches.

Keywords: Phase-field, Simulation, Microstructure, Spheroidal cast iron, Elastic mechanical properties

1. Introduction

Cast iron, a material in use for over six centuries, finds applications in various fields, including automobile parts, windmill rotor hubs, and machine structural components, owing to its outstanding combination of castability and mechanical properties [1, 2]. Spheroidal graphite iron (SGI), also known as ductile cast iron, is a more recent development from the 1940s, offering excellent mechanical properties and good recyclability at a competitive price [1–3]. The mechanical properties are intricately linked to the microstructure, which in turn is controlled by process parameters, such as chemical concentrations, cooling conditions, and inoculation [2, 4]. In this study, the correlation between process parameters, microstructural properties, and elastic-mechanical properties are investigated numerically by combining phase field simulations with the asymptotic homogenization technique.

The phase field (PF) method is considered the most powerful tool for describing spatial and temporal microstructure evolution in modern materials science and engineering [5–7]. The diffuse

interface description based on continuous order parameters avoids explicit tracking of interfaces and junctions. Thanks to corrections in the thin-interface limit [8, 9] and minimization of the discretization error [10], quantitative and accurate PF results can nowadays be obtained at the microstructure scale of technical relevance. Important steps toward application to complex engineering alloys and processes have been the generalization to multicomponent and multiphase systems (MMPF) and the coupling to CALPHAD-based thermodynamic and diffusion data [11–13]. With advancements in software and computing power, 3D simulation of complex materials processes has become feasible at the size of representative volume elements. In Integrated Computational Materials Engineering (ICME), MMPF simulations serve as a crucial link between processing and properties [6,14,15].

Despite this progress, application to spheroidal cast iron (SGI) remains challenging, due to the significant volumetric change during transformation of interstitial carbon to graphite and the complex implications on silicon and other substitutional elements [16, 17]. To the best of our knowledge, the volumetric MMPFF (Vol-MMPF) model by Eiken and Böttger [18], implemented in the MICRESS® software [19] is the only existing model that enables quantitative PF simulations of multicomponent SGI grades. In previous studies, the model was validated against experimental data and proved successful in studying microstructure evolution and microsegregation phenomena during solidification [20–23]. In this work, 3D Vol-MMPF simulations of hypoeutectic SGI grades are extended to ambient temperature, including for the first time the eutectoid decomposition of austenite into ferrite and graphite. In a case study, variations are performed with respect to chemical composition and process conditions.

The obtained as-cast structures can be considered as two-phase composites, characterized by graphite nodules of varying number, size, sphericity and volume fraction distributed in a polycrystalline, fully ferritic matrix. In a post-processing step, the effective elastic mechanical properties of the virtual as-cast microstructures are evaluated using the asymptotic homogenization method implemented in HOMAT [24, 25]. The fundamental workflow which bridges process, microstructure and properties proved successful in previous ICME studies for aluminium alloys [26] and steels [14, 15, 27], but not yet for SGI. Homogenization analysis of SGI has been performed on elementary cells [4, 28] and Finite Element meshes reconstructed from experimental data [29]. Different first-order mean field equations exist, which describe Young's modulus as linear function of graphite volume fraction [4, 30, 31], however with significant deviations in slope.

The primary aim of this study is to evaluate the homogenized elastic properties derived from simulated microstructures, validating their correlation with graphite volume fraction and examining the influence of additional morphological factors. This research is part of the broader DFG project, which seeks to establish a comprehensive process-structure-property workflow for SGI [32].

The paper is structured as follows: section 2 describes the model and input data, while section 3 presents the reference simulation and parameter variations. In section 4, the homogenized elastic mechanical properties are correlated to the characteristic graphite properties and compared to mean-field estimates and experimental data from literature. Finally, section 5 provides conclusions and an outlook.

2. Model description

2.1. General framework

Simulations are performed using the volumetric MMPF model by Eiken and Böttger [18] implemented in MICRESS® (pre-release version 7.25). The model is an extension of the standard MMPF model by Eiken et al [11, 12] and enables microstructure simulations in both 2D and 3D with an arbitrary number of phases and components under consideration of volume change. Thermodynamic, diffusion and volumetric data are evaluated during simulation from CALPHAD databases TCFE9 and MOBFE4 via Thermo-Calc's TQ-Interface [33, 34]. To enable quantitative predictions, the governing equations are corrected in the thin-interface limit and solved with minimized discretisation error [10].

The model is based on a set of phase-fields, $\phi_{\alpha=1..\check{n}}(\vec{x},t)$, which map the spatial distribution of multiple grains (α=1..$\check{n}$). Each "grain" defines a region with a uniform phase state, such as liquid (LIQ), austenite (FCC), graphite (GRA) and ferrite (BCC). Solid grains are further characterized by a uniform crystallographic orientation. The phase-field value represents the local mole fraction of the grain. A value of unity corresponds to the bulk of the grain, while the interfaces are defined by a smooth, continuous transition to zero. The composition vector field $\vec{c}(\vec{x},t)$ maps the concentrations c^i of the alloying elements carbon (C) and silicon (Si). Within the diffuse interface regions, these mixture concentrations are partitioned into phase-specific concentrations c^i_α. A special feature of the Vol-MMPF model is that all entities are formulated in terms of mole fractions:

$$\phi_\alpha = \frac{n_{\alpha,mol}}{n_{mol}}, \ldots c^i = \frac{n^i_{mol}}{n_{mol}}, \ldots c^i_\alpha = \frac{n^i_{\alpha,mol}}{n_{\alpha,mol}} \quad (1)$$

In this equation n_{mol} denotes the local number density of moles, while $n_{\alpha,mol}$ refers to the mole number density in a specific grain.

2.2. Modelling of nucleation

New grains of negligible size are formed if the local thermodynamic undercooling at a potential nucleation site exceeds a specified critical nucleation undercooling. Nucleation conditions are specified individually for each phase. For primary FCC, nucleation is defined with a low undercooling of ΔT_{crit} = 1 K in one of the domain corners. Additional FCC grains may nucleate at the liquid-graphite interface with a high undercooling of ΔT_{crit} = 50 K. BCC nucleation at the GRA-FCC interface is modelled with an estimated undercooling of ΔT_{crit} = 20 K and a shield distance of 10 µm from other BCC grains. Nucleation of graphite nodules is modelled on virtual seeds of varying sizes, randomly distributed in the melt according to a given seed-density function. The seeds represent potential nucleation sites with size dependent critical undercooling [35]. The seed density distribution (Figure 1) is modelled by a lognormal function, categorized into ten classes with radii ranging from 0.0188 µm to 0.1066 µm, corresponding to critical undercooling values in the range from ΔT_{crit} = 10 K to 80

K. Smaller seeds corresponding to irrelevant high undercooling values are excluded.

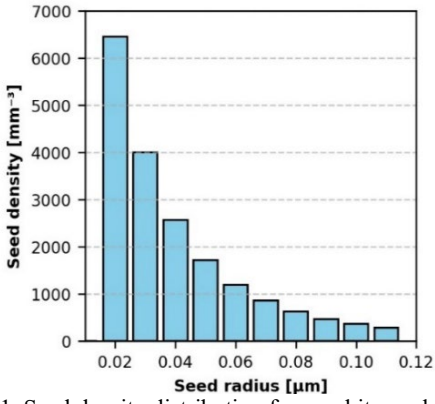

Fig. 1. Seed density distribution for graphite nucleation

The total seed density of N_{sd} = 3.1 ·10⁴·mm⁻³ has been calibrated through iterative simulations of the original six-component cast iron grade to a reference experiment, systematically varying the seed density until the resulting nodule counts aligned [36]. Depending on the process-specific thermodynamic undercooling, different nodule counts are predicted based on the same seed distribution function.

2.3. Modelling of growth

The temporal evolution of the multiphase structure is described by the following set of differential MPF equations, derived from an overall free energy functional [11, 12].

$$\dot{\phi}_\alpha = \sum_\beta^{\check{n}} \left[M_{\alpha\beta} \left(b_{\alpha\beta}\, \Delta g_{\alpha\beta} - \sigma_{\alpha\beta}\, K_{\alpha\beta} + \sum_\gamma^{\check{n}} J_{\alpha\beta\gamma} \right) \right] \tag{2}$$

$$\text{with } b_{\alpha\beta} = \frac{\pi}{\eta} (\phi_\alpha + \phi_\beta) (\phi_\alpha\, \phi_\beta)^{0.5} \tag{3}$$

$$K_{\alpha\beta} = \frac{1}{\check{n}} \left[\frac{\pi^2}{\eta^2} (\phi_\beta - \phi_\alpha) + (\nabla^2\phi_\beta - \nabla^2\phi_\alpha) + A_{\alpha\beta} \right] \tag{4}$$

$$J_{\alpha\beta\gamma} = \frac{1}{\check{n}} \left[\left(\frac{\pi^2}{\eta^2} \phi_\gamma + \nabla^2\phi_\gamma \right) \cdot (\sigma_{\beta\gamma} - \sigma_{\alpha\gamma}) + A_{\alpha\beta\gamma} \right] \tag{5}$$

where ň denote the number of locally interacting grains and η the diffuse interface thickness. The thermodynamic driving force $\Delta g_{\alpha\beta}$ is evaluated as function of composition and temperature from CALPHAD data. Its prefactor $b_{\alpha\beta}$ is a measure for the multi-phase-field gradient. The pairwise interface term $K_{\alpha\beta}$ corresponds to capillarity forces and $J_{\alpha\beta\gamma}$ to higher order junction torque. The interface mobility $M_{\alpha\beta}$ and the interface energy $\sigma_{\alpha\beta}$ depend on the normal growth direction and the crystal symmetry and orientation of the grains. The terms $A_{\alpha\beta}$ and $A_{\alpha\beta\gamma}$ summarize complex anisotropic derivatives of the interface energy $\sigma_{\alpha\beta}$, detailed in [12]. Graphite interfaces are modelled by an effective multi-faceted anisotropy with 50 c-type facets forming a spheroidal Wulff shape, see Figure 2.

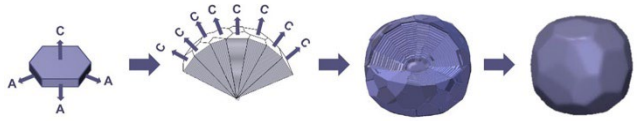

Fig. 2. Effective multi-faceted anisotropy for spheroidal graphite [21]

This anisotropy model, as well as mean values σ_0, M_0 and corresponding anisotropy coefficients δ_σ and δ_M (given in Table 1), are adopted from previous studies [20–23]. The added interfacial properties of BCC are estimates and still require validation.

Table 1.
Phase-specific interface properties

Phases	σ_0	M_0	Model	δ_σ	δ_M
-	[Jm^{-2}]	[m^4(Js)$^{-1}$]	-	-	-
LIQ-FCC	0.17	1 10^{-08}	cubic	0.05	0.05
LIQ -GRA	1.80	1·10^{-13}	faceted	0.81	0.60
FCC-FCC	0.05	1·10^{-17}	-	-	-
FCC-BCC	0.06	2·10^{-14}	-	-	-
FCC- GRA	1.50	3·10^{-15}	faceted	0.20	0.50
BCC-BCC	0.07	1·10^{-17}	-	-	-
BCC- GRA	1.00	1·10^{-12}	faceted	0.81	0.60
GRA-GRA	1.00	1·10^{-17}	-	-	-

Note that the mobilities of the diffusion-controlled phase-interfaces are corrected in the thin-interface limit [8, 9] during simulation.

2.4. Solute diffusion and partitioning

Diffusion of the elements C and Si (including cross dependencies) in the different phases is modelled by:

$$\dot{\vec{c}} = n_{mol}^{-1} \left(\Sigma_\alpha \nabla \cdot n_{mol}\, \overline{\overline{D}}_\alpha \nabla\, \vec{c}_\alpha \right) + \vec{j}_{atc} \tag{6}$$

where $\overline{\overline{D}}_\alpha$ is the phase-specific diffusion matrix and $\vec{j}_{atc}$ the anti-trapping current [8]. The evaluation of the phase-specific diffusion matrices, as well as the partitioning of the mixture concentrations $\vec{c}$ into individual phase-specific concentrations $\vec{c}_\alpha$ at the interfaces is calculated based on CALPHAD data. Modelling the interplay between interstitial and substitutional diffusion in FCC and BCC is a major challenge. The slow substitutional diffusion of Si is modelled with para-equilibrium conditions [37] at the FCC-BCC interface and without considering off-diagonal coefficients in the bulk. Interstitial diffusion of C is modelled with full diffusion matrix. The inherent mole flux changes the local mole number density and thus require a recalculation of the composition vector at the end of each explicit time step Δt:

$$\vec{c}(t+\Delta t) = \left[\vec{c}(t) + \dot{\vec{c}}(t) \cdot \Delta t \right] \frac{n_{mol}(t)}{n_{mol}(t) + \dot{n}_{mol}^{diff}(t) \cdot \Delta t} \tag{7}$$

$$\text{with } \dot{n}_{mol}^{diff}(\vec{x},t) = \nabla\, j_A^C(\vec{x},t) \tag{8}$$

Note that concentrations are converted to wt% for input and output.

2.5. Process conditions

Process specific heat extraction $\dot{q}_{ex}(t)$ is modelled from the casting modulus M and the mould diffusibility D_m, based on Chvorinov's rule for sand castings [38]:

$$\dot{q}_{ex}(t) = \frac{D_m}{M} \cdot \frac{T(t) - T_A}{\sqrt{t}} \quad \text{with} \quad D_m = \sqrt{\frac{\lambda_m \rho c_{Pm}}{\pi}} \tag{9}$$

The model assumes that heat diffusion inside the casting is fast compared to heat diffusion inside the mould. T(t) denotes the homogeneous temperature inside the casting and T_A=25°C the ambient temperature. The casting modulus M = V/A = 11 mm refers to a model casting with standard Y2 geometry. The definition of the heat diffusibility D_m in equation (9) is adopted from Fredriksson and Svensson [38]. It accounts for the thermal properties of the furan sand mould, but should not be confused with the standard thermal diffusivity. Since Micress version 7.25 does not yet support a temperature-dependent input, a constant value D_m = 665 $JK^{-1}m^{-2}S^{-0.5}$ was approximated based on an average heat conductivity λ_m = 0.884 $Wm^{-1}K^{-1}$ and an average volumetric heat capacity ρc_{Pm}= 1.57 ·10^6 $Jm^{-3}K^{-1}$. Starting from an initial temperature of 1313 °C, the temperature change is calculated from the following heat balance:

$$\dot{T}(t) = \frac{h_{Lat}(\{\phi_\alpha\}) - \dot{q}_{ex}(t)}{\rho c_p} \tag{10}$$

where $h_{Lat}(\{\phi_\alpha\})$ is the growth-related latent heat release and ρc_P the mean volumetric heat capacity of the casting, both evaluated during simulation from CALPHAD data.

2.6. Volume change

Volume density is calculated by multiplying the molar number density with local molar volume v_{mol} evaluated from CALPHAD data. A homogenised volume change is obtained by iterative relaxation of temporary gradients under consideration of mass conservation:

$$j^{\tau}_{mol} = v^{-1}_{mol} M_V \nabla (n^{\tau}_{mol} v_{mol}) \tag{11}$$

$$n^{\tau+1}_{mol} = n^{i}_{mol} + \nabla \cdot j^{\tau}_{mol} \tag{12}$$

$$\vec{c}^{\,\tau+1} = \frac{\vec{c}^{\tau} n^{\tau}_{mol} + \nabla \cdot (\vec{c}^{\tau} j^{\tau}_{mol})}{n^{\tau+1}_{mol}} \tag{13}$$

The homogenizing mole fluxes j^{τ}_{mol} can be associated with viscoplastic creep on a timescale $\tau \ll t$. The relaxation coefficient M_V is a numerical parameter determined by a stability criterion. Equation (12) is solved iteratively until a convergence criterion is reached. The recalculation of the composition vector after each iteration in Equation (13) accounts for advective solute fluxes, which present the dominant mechanism for transport of substitutional elements at the FCC/GRA interface [2].

2.7. Evaluation of graphite characteristics

After simulation, the characteristics of the graphite precipitates are evaluated from the final microstructure. The volume fraction (f_{Vol}), the total number of nodules in the RVE (N_{RVE}), the nodule density per volume (N_V),), as well as the diameter D, the volume V and the surface area A of the nodules are all direct output of MICRESS®. The nodule density per area (N_A) is calculated by equation (14) [21] and the mean sphericity (Ψ) by equation (15) [39].

$$N_A = N_V D \tag{14}$$

$$\Psi = \sqrt[3]{36\pi V^2}/A \tag{15}$$

2.8. Homogenisation

The software HOMAT [24, 25] is based on the asymptotic homogenization method and generally allows determination of effective properties from heterogonous structures in a 3D RVE. In this study, it is used as a post-processing tool to determine effective elastic properties from the final as-cast microstructures simulated with MICRESS®. The transfer from MICRESS® to HOMAT involves two steps: first, converting the file format of the grain output from MICRESS® to VTK (Visualization Toolkit), and second generating a finite-element mesh using the script Mesh2Homat [40]. The as-cast structures are solid two-phase composites, characterized by graphite nodules of varying number, size and sphericity, distributed in a polycrystalline ferrite matrix. For both pure phases, isotropic elastic behaviour is assumed, with Young's moduli and Poisson ratios adopted from Bonora et al. [41] for ferrite, and from Kosteski et al. [42] for graphite, see Table 2.

Table 2.
Elastic properties of pure phases [41], [42]

Phases	Young's modulus	Poisson's ratio
Ferrite	210 GPa	0.3
Graphite	15 GPa	0.3

3. Simulation Results

This section starts with a description of the reference simulation, performed based on equations and parameters from section 2. Subsequently, the impact of process variations on the morphological characteristics of the graphite precipitates is studied.

3.1. Reference simulation

The case study is conducted on a slightly hypoeutectic F-C-Si-(Mg) model alloy, detailed in Table 3. Mg is not directly modelled, but its spheroidizing effect is implicitly considered in the graphite interfacial properties (Table 1).

Table 3.
Nominal composition of the reference simulation

Fe	C	Si	(CE)	unit
94.60	3.50	1.90	4.03	wt%

Simulations are performed in a cubic RVE with symmetric boundary conditions. The side length of a = 200 µm corresponds approximately to half of the size of a FCC grain, evaluated from micrographs of a Y2 sample, provided by the foundry institute of the RWTH Aachen as part of a common DFG project [32]. A numerical parameter study identified 1.75-µm cell spacing as a good balance between computational efficiency and accuracy. The low resolution is feasible due to a submodel that calculates initial curvatures from fractions and a special FD scheme that minimizes discretization error [10]. A higher resolution would be needed for accurately resolving the initial dendrite tips, which, however, is of minor importance for the present study. Figure 3 illustrates the predicted phase sequence at six distinct stages of microstructure evolution from pouring to final as-cast structure and Figure 4 presents the corresponding 3D structures. The simulation starts from pure liquid at 1313°C. Austenite (FCC) nucleates at 1194.2 °C in the corner of the domain and grows with dendritic morphology (I). Below 1161.13 °C, graphite begins to nucleate from the liquid and grows with spheroidal (multi-facetted) morphology (II). Initial graphite nucleation is favoured close to the FCC interface, where the C content is highest. Vice versa, graphite nucleation favours FCC growth. After impingement, FCC encapsulates the graphite nodules. Both phases continue to grow in a divorced eutectic transformation, controlled by carbon diffusion through the FCC shell (III). The intermediate structure after solidification is characterized by graphite nodule embedded in a FCC matrix (IV). Nucleation of BCC at the graphite interface starts at 787.85°C. After encapsulation, growth is controlled by interstitial C diffusion through the BCC shell (V). At about 610 °C the final as-cast microstructure is reached (VI), which remains unchanged until ambient temperature. Small amounts of cementite that may precipitate toward the end of the eutectoid transformation are neglected in this case study.

In the following subsections, results from simulations with variation of casting modulus, seed density, Si content and C content are presented.

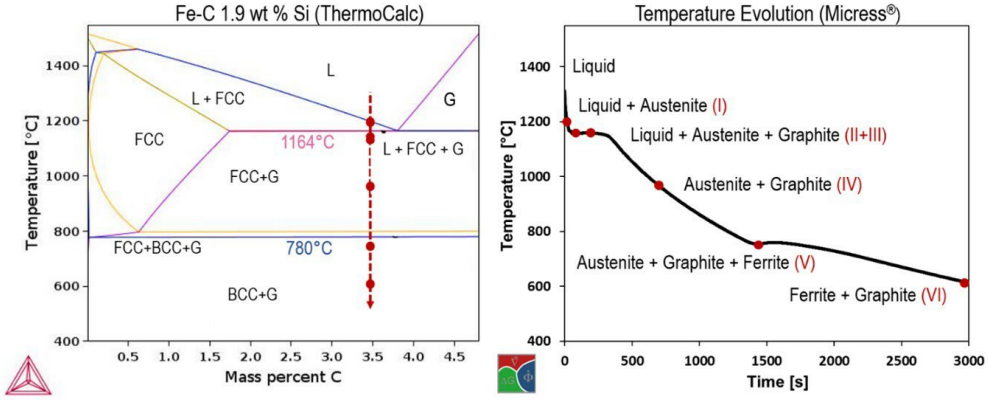

Fig. 3. Phase sequence of hypoeutectic SGI at six distinct stages from pure melt to final as cast structure

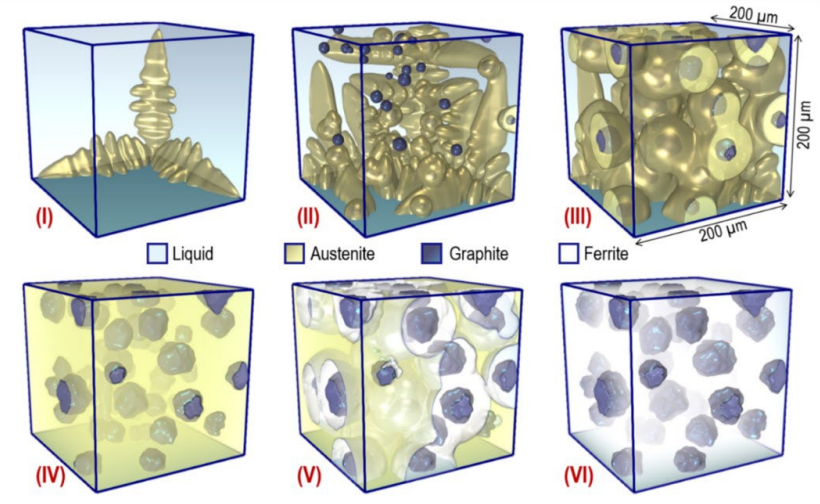

Fig. 4. Simulated microstructure evolution from beginning dendritic growth in pure melt to final cast structure

3.2. Variation of casting modulus

In the first series of simulations, the casting modulus (M) is varied in the range from 8 mm to 20 mm. Figure 5 shows the simulated temperature evolution, while Figure 6 illustrates the trend of the characteristic graphite properties. As expected, increasing M significantly extends the process time. Despite this, the graphite volume fraction remains nearly constant. However, the reduced undercooling results in lower number of nodules, which consequently exhibit a larger diameter. The mean sphericity decreases. Note that the depicted nodule number N_{RVE} refers to the absolute number of nodules in the RVE, while corresponding nodule densities values N_A and N_V are quantified in Table 4.

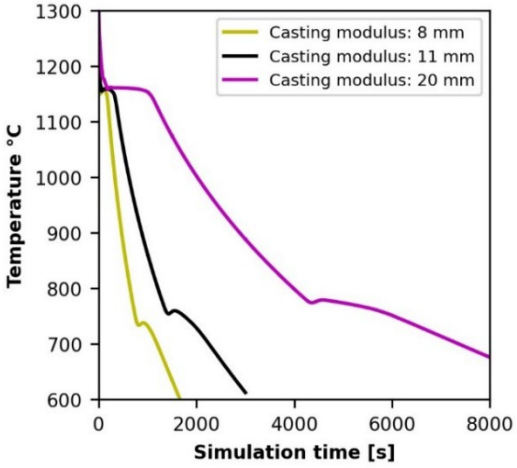

Fig. 5. Temperature curves from varying casting modulus

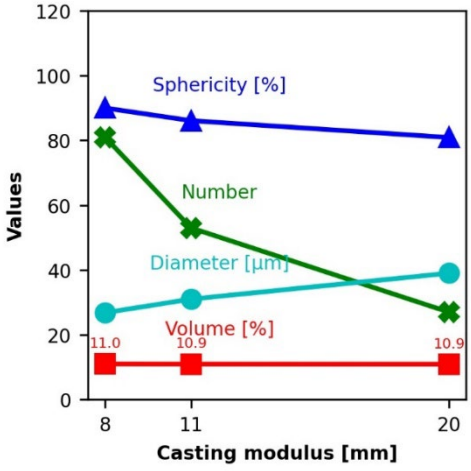

Fig. 6. Graphite properties from varying casting modulus

3.3. Variation of nucleation seed density

In the second series of simulations, the total seed density is varied from $N_{sd} = 2 \cdot 10^4$ mm^{-3} to and $9.5 \cdot 10^4$ mm^{-3}. Figure 7 shows the temperature evolution and Figure 8 the graphite characteristics. An increased number of potential nucleation sites for graphite results in higher nodule numbers and decreased eutectic undercooling. The process time and the graphite fraction remain almost unaffected. Consequently, the diameter decreases, while the sphericity increases. Interestingly, the eutectoid transformation shifts to higher temperatures, which might be explained by the increased number of nodules, providing more nucleation sites for BCC. The evaluated graphite characteristics are given in Table 4.

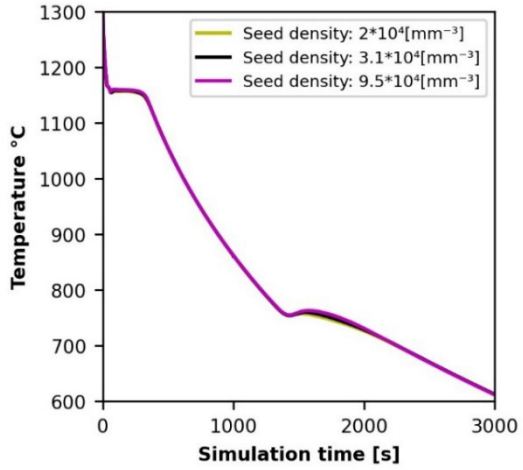

Fig. 7. Temperature curves from varying seed densities

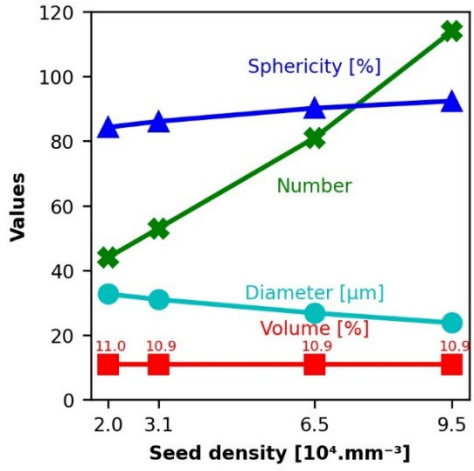

Fig. 8. Graphite properties from varying seed densities

3.4. Variation of silicon content

The nominal concentration of silicon is varied in the range from 1.7 wt% to 2.5 wt%. As the C content is kept constant, the CE increases with Si content. Figure 9 shows that Si slightly rises the eutectic transformation temperature and, more significantly, the eutectoid temperature. However, a closer analysis reveals that the initial undercooling during primary solidification increases, which

can be explained by the decrease of the FCC liquidus temperature. An enhanced growth restriction due to Si redistribution may further contribute to this effect. The increased undercooling enables graphite nucleation on smaller seeds, requiring higher nucleation undercooling. Figure 10 illustrates the slight increase in nodule number. Since the graphite fraction remains unchanged, it is correlated with a decrease in mean diameter. In contrast, the sphericity of the nodules slightly increases.

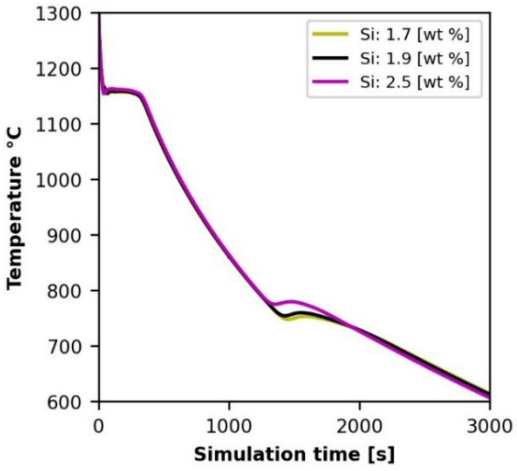

Fig. 9. Temperature curves from varying Si contents

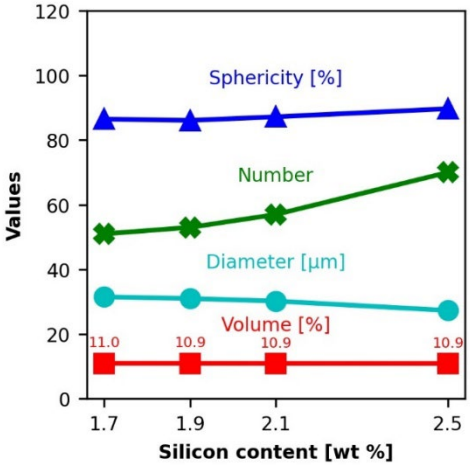

Fig. 10. Graphite characteristics from varying Si contents

3.5. Variation of carbon content

In the fourth series of simulations, the nominal carbon concentration is varied from 3.3 wt% to 3.6 wt%. The temperature evolution shown in Figure 11 indicates that increasing carbon content raises the liquidus temperature and slightly shifts the entire cooling curve upward. Figure 12 illustrates the effect of carbon content on the graphite characteristics. In contrast to the previously discussed variations, a significant increase in graphite volume fraction is observed at higher carbon levels. Despite this increase in volume, the average nodule diameter decreases due to the simultaneous increase in nodule number. As in the previous variations, sphericity exhibit an inverse correlation with the nodule diameter. The detailed values for nodule density (N_A, N_V) are provided in Table 4.

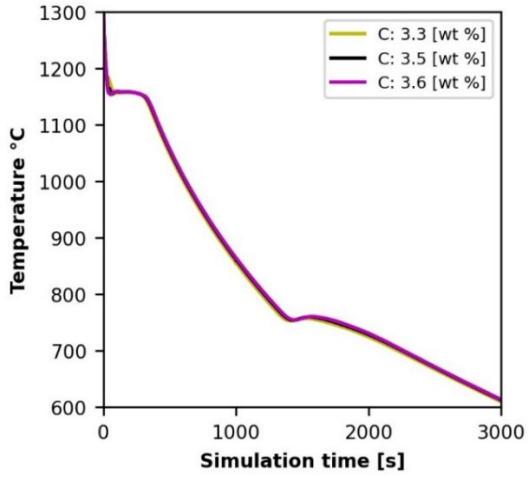

Fig. 11. Temperature curves from varying C contents

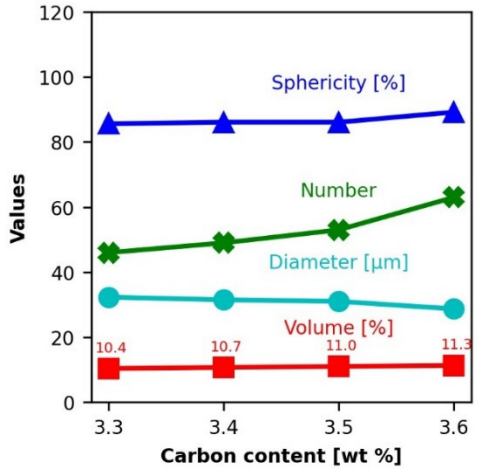

Fig. 12. Graphite characteristics from varying C contents

Table 4.
Graphite characteristics and elastic mechanical properties from varying process conditions

		N_{RVE}	N_V	N_A	D	f_{vol}	Ψ	E	G	υ
Variations	Values		[mm^{-3}]	[mm^{-2}]	[µm]	[%]	[%]	[GPa]	[GPa]	
Casting modulus M [mm]	8	81	10125	271	26.8	11.0	90.0	167.84	64.91	0.2892
	11	53	6625	205	31.0	10.9	86.1	167.51	64.64	0.2890
	20	27	3375	132	39.0	10.9	80.9	167.88	64.44	0.2879
Seed density N_{sd} [10^4 mm^{-3}]	2.0	44	5500	180	32.7	11.0	84.3	166.64	64.53	0.2892
	3.1	53	6625	205	31.0	10.9	86.1	167.51	64.64	0.2890
	6.5	81	10125	271	26.8	10.9	90.2	167.53	64.95	0.2897
	9.5	114	14250	339	23.8	10.9	92.4	168.60	65.01	0.2889
Silicon content Si [wt%]	1.7	51	6375	201	31.5	11.0	86.5	167.30	64.71	0.2891
	1.9	53	6625	205	31.0	10.9	86.1	167.51	64.64	0.2890
	2.1	57	7125	215	30.2	10.9	87.2	167.61	64.83	0.2891
	2.5	70	8750	239	27.3	10.9	89.7	168.00	64.93	0.2890
Carbon content C [wt%]	3.3	46	5750	186	32.3	10.4	85.5	169.04	65.20	0.2896
	3.4	49	6125	193	31.5	10.7	86.1	168.00	64.90	0.2890
	3.5	53	6625	205	31.0	11.0	86.1	167.51	64.64	0.2890
	3.6	63	7875	226	28.7	11.3	89.2	166.77	64.51	0.2892

4. Homogenised mechanical properties

The final two-phase structures are characterized by graphite nodules with varying properties embedded in a fully ferritic matrix. In a post-processing step, the elastic mechanical properties are evaluated based on asymptotic homogenization. In this section, these properties are first discussed in correlation with the graphite characteristics (subsection 4.1) and then compared to mean-field estimates and experimental data from literature (subsection 4.2).

4.1. Correlation of elastic and graphite

By altering the metallurgical input parameters, RVE with varying graphite characteristics have been generated (see Section 3). The last three columns in Table 4 present the homogenized elastic mechanical properties evaluated from the four series of parameter variations, specifically the Young's modulus (E), the shear modulus (G), and the Poisson's ratio (ν).

The correlation between various graphite characteristics and the moduli is visualized in Figure 13(a-d) for Young's modulus and Figure 14(a-d) for shear modulus. As anticipated, the moduli primarily depend on the graphite volume fraction. An increase in the graphite volume fraction by 0.9% results in a decrease of 2.27 GPa in Young's modulus, which can be explained by the lower elasticity of graphite compared to ferrite. Figures 13(a) and 14(a) illustrate that this change is primarily due to the variation of carbon content, while other variations have additional but smaller impact.

Figures 13(b-d) and 14(b-d) demonstrate that at a constant carbon content (i.e., constant graphite fraction), the moduli tend to increase with nodule number and sphericity but decrease with nodule diameter. All three graphite characteristics are closely related. It is hypothesized that smaller nodules generally exhibit a larger sphericity, which could be the major cause for the increase in the elastic properties. Young's moduli and shear moduli exhibit similar, though not identical, trends. The Young's modulus evaluated from the RVE with smallest nodule number strongly deviates from the general trend. This is likely due to insufficient statistics and resulting effective anisotropy, leading to deviations from the standard isotropic relationship $E = 2G(1+\nu)$.

Overall, it must be concluded that the range of elastic properties, obtained from the various variations of the ferritic SGI microstructures is quite narrow. Values for Young's modulus range from E =166.64 to 169.04 GPa and for shear modulus from G = 64.44 GPa to 65.20 GPa, while the Poisson's ratio (ν =0.2879 to 0.2897) hardly changes at all. An explanation may be that the effects of morphology and volume fraction partially compensate each other. Increasing the carbon content increases the graphite fraction, but simultaneously also the nodule number and the sphericity, which have opposing effects.

4.2. Comparison with mean field models and experimental data

In Figure 15, three different mean-field approaches from literature are compared to the results of the present study. All approaches describe the Young's modulus as a linear function of the graphite volume fraction:

$$E = E_{BCC} + m_E(E_{BCC}, E_{GRA}) \cdot f_{Vol} \quad (16)$$

Identical values for E_{BCC} and E_{GRA} from Table 2 are used. A slope of m_E = -3.86 is found to best fit the results of the present case study. A simple volume averaging ($(1-f_{vol}) \cdot E_{BCC} + f_{vol} \cdot E_{GRA}$) results in a significantly lower slope of m = -1.95 GPa. The Mori-Tanaka approach for spherical particles discussed in [4] yields a slope of m_E = -3.22 GPa. Best agreement (m_E = -3.49 GPa) is found by modelling graphite as spherical inclusions in a dilute composite according to Grimvall [30]. However, the deviations of all estimates are large compared to the small range of variation observed by simulation. In addition, two experimental values from

literature are plotted in Figure 15. The Young's modulus of E = 169 GPa measured by Speich et al [31] for Fe- C 3.69 wt% - Si 2.33 wt% with f_{vol} = 10.5% shows excellent agreement with the simulated results. The value E = 172 GPa measured by Fernandino et al [29] for Fe- C 3.32 wt% - Si 2.36 wt% with f_{vol} = 11.6% deviates by about 6.7 GPa.

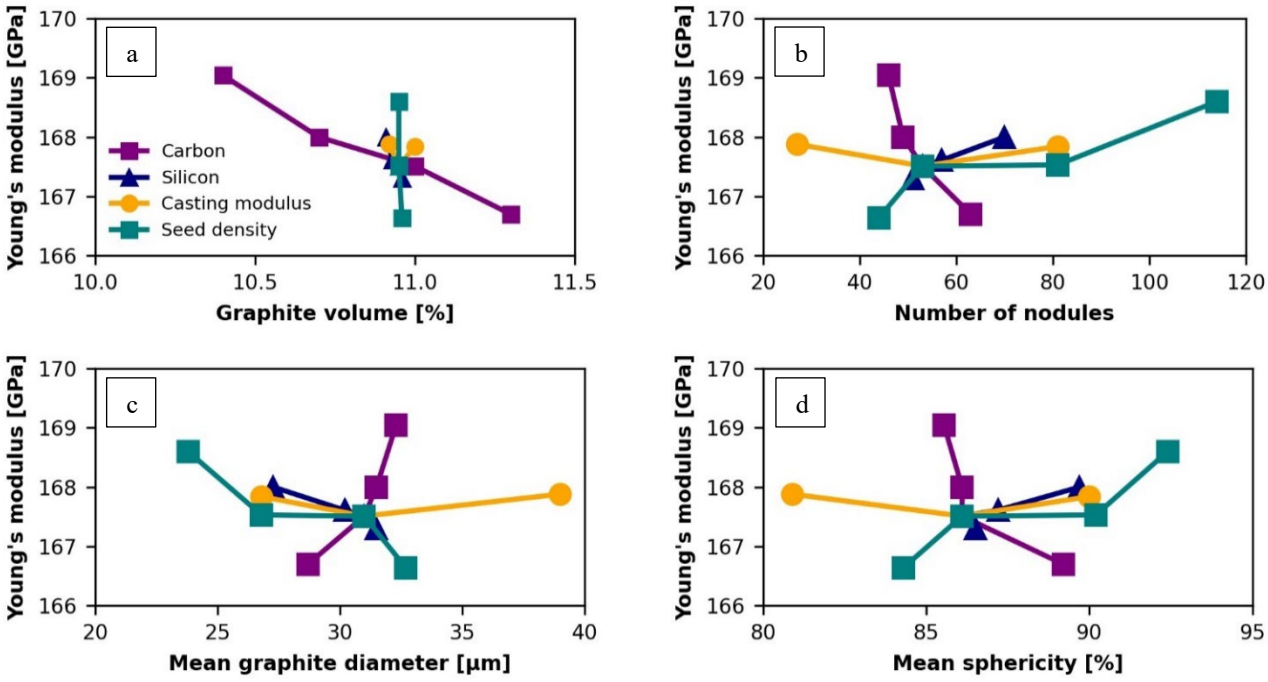

Fig. 13. Young's modulus vs graphite characteristics a) graphite volume b) number of nodules c) mean graphite diameter and d) mean sphericity

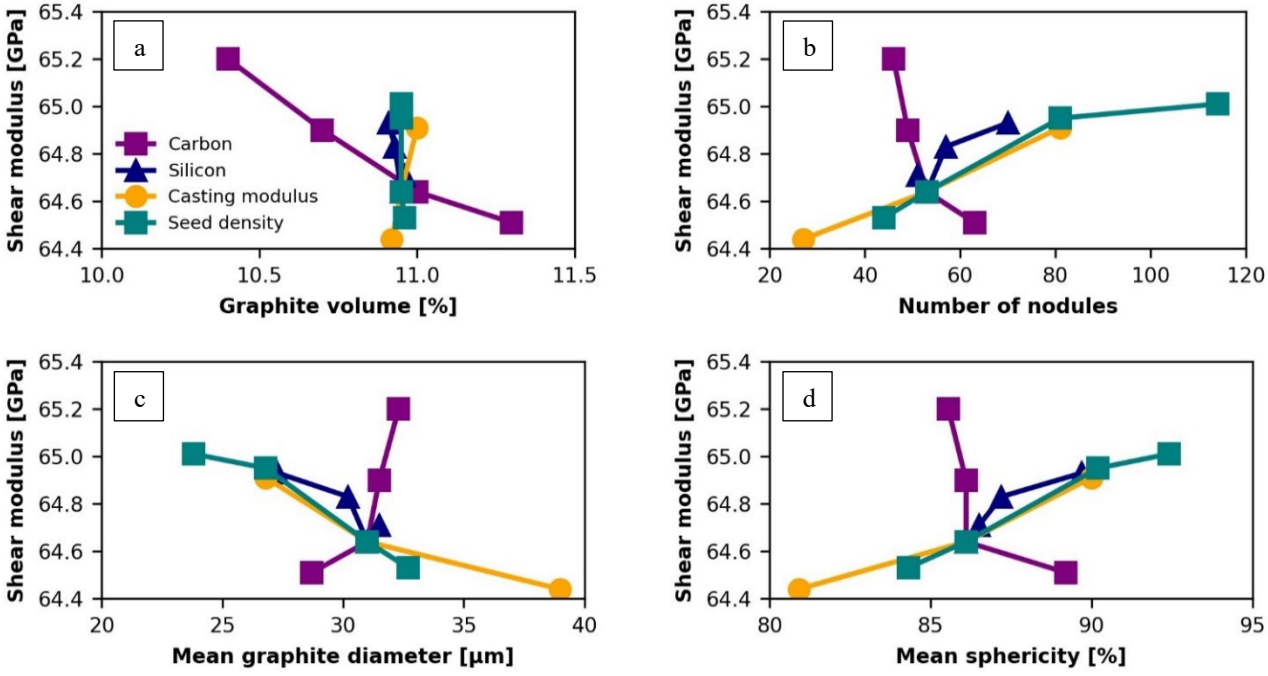

Fig. 14. Shear modulus vs graphite characteristics a) graphite volume b) number of nodules c) mean graphite diameter and d) mean sphericity

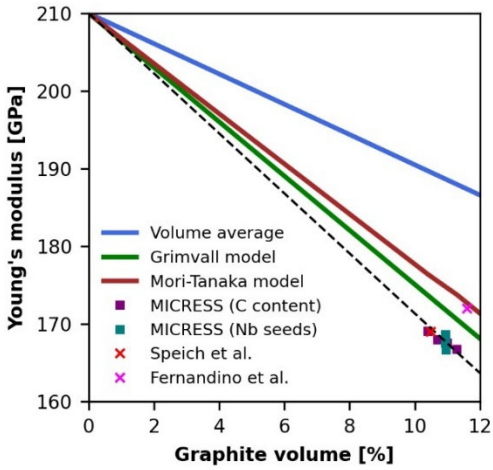

Fig. 15. Comparison with linear mean-field estimates and experimental data from literature

5. Conclusion and outlook

The correlation between characteristics of graphite nodules and elastic-mechanical properties of spheroidal graphite iron was investigated by combination of multi-phase-field simulations and asymptotic homogenisation. 3D microstructure evolution of a near eutectic SGI was for the first time extended to the as-cast structure, consisting of graphite nodules embedded in a ferrite matrix.

Variation of the metallurgical process parameters revealed that increase in a) cooling rate, b) nucleation seed density, c) silicon content, and d) carbon content results in increased nodule number and mean sphericity, while the mean nodule diameter decreases. These three graphite characteristics are closely related in all variations. Only changing the carbon content causes a change in the graphite volume fraction and thus a significant change in the homogenized elastic mechanical properties. The observed correlation of Young's modulus and graphite fraction significantly differs from standard mean-field estimates. In contrast, comparison of the predicted Young's modulus with experimental data from literature were revealed good agreement.

However, it must be emphasized that the predicted range of elastic properties is narrow. Varying the carbon content from 3.3 wt% to 3.6 wt% decreases the Young's modulus by only 2.27 GPa and the shear modulus by 0.69 GPa, while the Poisson's ratio remains almost unchanged. The results suggest that the simultaneous effects of increased graphite volume and increased nodule number may partially compensated each other. Further investigation is needed to determine if varying the graphite fraction independently would yield a more pronounced impact. It is noteworthy that additional variation of the graphite distribution based on a bi-modal nucleation function (not presented in this paper) did not significantly alter the elastic properties.

In the further course of the project, a similar workflow will be employed to predict the mechanical properties of SGI with a mixed ferrite and pearlite matrix.

Acknowledgements

We acknowledge funding in the framework of the DFG- project "Experimentally based modelling of the correlation between metallurgical process control, 3D microstructure evolution, and mechanical properties of pearlitic cast iron with spheroidal graphite" under grant number: 504974025.

References

[1] Stefanescu, D.M. (2018). A history of cast iron. In George E. Totten (Eds.), *ASM Handbook* (Vol. 1A, pp. 3–11). ASM International.

[2] Lacaze, J., Sertucha, J., Castro-Román, M. J. (2021). *A contemporary monograph on silicon cast irons microstructure-From atom scale to casting* (online).

[3] Liu, J. H., Yan, J. S., Zhao, X. B., Fu, B. G., Xue, H. T., Zhang, G. X., & Yang, P. H. (2020). Precipitation and evolution of nodular graphite during solidification process of ductile iron. *China Foundry*, 17(4), 260-271. DOI:10.1007/s41230-020-0042-2.

[4] Andriollo, T. & Hattel, J. (2016). On the isotropic elastic constants of graphite nodules in ductile cast iron: Analytical and numerical micromechanical investigations. *Mechanics of Materials*. 96, 138-150. DOI: 10.1016/j.mechmat.2016.02.007.

[5] Tourret, D., Liu, H. & Lorca, J. (2022). Phase-field modeling of microstructure evolution: Recent applications, perspectives and challenges. *Progress in Materials Science.* 123, 100810, 1-19. https://doi.org/10.1016/j.pmatsci.2021.100810.

[6] Chen, L.Q. & Moelans, N. (2024). Phase-field method of materials microstructures and properties. *MRS Bulletin*. 49(6), 551-555. https://doi.org/10.1557/s43577-024-00724-7.

[7] Steinbach, I., Uddagiri, M., Salama, H., Ali, M.A. & Shchyglo, O. (2024). Highly complex materials processes as understood by phase-field simulations: Additive manufacturing, bainitic transformation in steel and high-temperature creep of superalloys. *MRS Bulletin*. 49, 583-593. DOI:10.1557/s43577-024-00703-y.

[8] Carré, A., Böttger, B. & Apel, M. (2013). Implementation of an antitrapping current for a multicomponent multiphase-field ansatz. *Journal of Crystal Growth.* 380, 5-13. DOI: 10.1016/j.jcrysgro.2013.05.032.

[9] Karma, A. (2001). Phase-field formulation for quantitative modeling of alloy solidification. *Physical Review Letters.* 87(11), 115701, 1-4. DOI:10.1103/PhysRevLett.87.115701.

[10] Eiken, J. (2012). The finite phase-field method - A numerical diffuse interface approach for microstructure simulation with minimized discretization error. *Materials Research Society Symposium Proceedings.* 1369, 62-68. Materials Research Society. DOI:10.1557/opl.2012.510.

[11] Eiken, J., Böttger, B. & Steinbach, I. (2006). Multiphase-field approach for multicomponent alloys with extrapolation scheme for numerical application. *Physical Review E - Statistical, Nonlinear, and Soft Matter Physics*. 73(6), 066122, 1-9. DOI:10.1103/PhysRevE.73.066122.

[12] Eiken, J. (2009). *A Phase-Field Model for Technical Alloy Solidification*. Shaker Verlag.
[13] Fries, S.G., Boettger, B., Eiken, J. & Steinbach, I. (2009). Upgrading CALPHAD to microstructure simulation: the phase-field method. *International Journal of Materials Research.* 100(2), 128-134. DOI: 10.3139/146.110013.
[14] Deepu, M.J. & Phanikumar, G. (2020). ICME Framework for Simulation of Microstructure and Property Evolution During Gas Metal Arc Welding in DP980 Steel. *Integrating Materials and Manufacturing Innovation.* 9(3), 228-239. DOI:10.1007/s40192-020-00182-4.
[15] Nomoto, S., Oba, M., Mori, K. & Yamanaka, A. (2017). Microstructure-based multiscale analysis of hot rolling of duplex stainless steel using various simulation software. *Integrating Materials and Manufacturing Innovation.* 6(1), 69-82. DOI:10.1007/s40192-017-0083-6.
[16] Lesoult, G., Castro, M. & Lacaze, J. (1998). Solidification of spheroidal graphite cast irons—I. Physical modelling. *Acta materialia*. 46(3), 983-995. https://doi.org/10.1016/S1359-6454(97)00281-4.
[17] Lacaze, J., Castro, M. & Lesoult, G. (1998). Solidification of spheroidal graphite cast irons—II. Numerical simulation. *Acta materialia*. 46(3), 997-1010. https://doi.org/10.1016/S1359-6454(97)00282-6.
[18] Eiken, J. & Böttger, B. (2018). A multi-phase-field Approach for Solidification with Non-negligible Volumetric Expansion—Application to Graphite Growth in Nodular Cast Iron. *Transactions of the Indian Institute of Metals.* 71(11), 2725-2729. DOI:10.1007/s12666-018-1427-4.
[19] MICRESS. (2024). *Multicomponent multi-phase-field software version 7.250.* Retrieved February 26, 2024, from https://micress.rwth-aachen.de/.
[20] Eiken, J. (2020). Calphad-based phase-field study of the interplay between spheroidal graphite growth and chemical segregation in ductile cast iron. In *IOP Conference Series: Materials Science and Engineering* (Vol. 861, No. 1, p. 012055). Institute of Physics Publishing. DOI:10.1088/1757-899X/861/1/012055.
[21] Eiken, J., Subasic, E. & Lacaze, J. (2020). 3D phase-field computations of microsegregation in nodular cast iron compared to experimental data and Calphad-based Scheil-prediction. *Materialia*. 9, 100538, 1-11. DOI: 10.1016/j.mtla.2019.100538.
[22] Horbach, L., Gebhardt, C., Zhang, J., Joseph, B. D., Bührig-Polaczek, A. & Broeckmann, C. (2024). The effect of silicon microsegregation on the mechanical properties of high silicon alloyed ductile cast iron under monotonous loading. *Heliyon*. 10(1), e23904, 1-19. DOI: 10.1016/j.heliyon. 2023.e23904.
[23] Eiken, J. & Lacaze, J. (2017). Microsegregation build-up during solidification of nodular cast iron - Phase-field simulation versus experimental information. Microsegregation build-up during solidification of nodular cast iron-Phase-field simulation versus experimental information. In *Proceedings of the 5th Decennial International Conference on Solidification Processing, Old Windsor, UK* (pp. 25-28).
[24] Access e.V. (1996). HOMAT-Docs. Retrieved from https://docs.micress.rwth-aachen.de/homat/.
[25] Laschet, G. (2002). Homogenization of the thermal properties of transpiration cooled multi-layer plates. *Computer Methods in Applied Mechanics and Engineering.* 191(41-42), 4535-4554. https://doi.org/10.1016/S0045-7825(02)00319-5.
[26] Zhou, B., Laschet, G., Eiken, J., Behnken, H. & Apel, M. (2020). Multiscale solidification simulation of Sr-modified Al-Si-Mg alloy in die casting. In *IOP Conference Series: Materials Science and Engineering*, 22-23 June 2020 (Vol. 861, 1-8). Institute of Physics Publishing. DOI:10.1088/1757-899X/861/1/012034.
[27] Laschet, G. & Apel, M. (2010). Thermo-elastic homogenization of 3-D steel microstructure simulated by the phase-field method. *Steel Research International.* 81(8), 637-643. DOI:10.1002/srin.201000077.
[28] Boccaccini, A.R. (1997). Young's modulus of cast-iron as a function of volume content, shape and orientation of graphite inclusions. *International Journal of Materials Research.* 88(1), 23-26. DOI:10.3139/ijmr-1997-0005.
[29] Fernandino, D.O., Cisilino, A.P. & Boeri, R.E. (2015). Determination of effective elastic properties of ferritic ductile cast iron by computational homogenization, micrographs and microindentation tests. *Mechanics of Materials.* 83, 110-121. DOI: 10.1016/j.mechmat.2015.01.002.
[30] Grimvall, G. (1997). Cast iron as a composite: conductivities and elastic properties. *Advanced Materials Research*. 4-5, 31-46. DOI: 10.4028/www.scientific.net/amr.4-5.31.
[31] Speich, G.R., Schwoeble, A.J. & Kapadia, B.M. (1980). Elastic moduli of gray and nodular cast iron. *Journal of Applied Mechanics.* 47(4), 821-826. DOI:10.1115/1.3153797.
[32] Bührig-Polaczek, A., Broeckmann, C. & Eiken, J. (2023). Experimentally supported modelling of the correlation between metallurgical process control, 3D microstructure development and mechanical properties of pearlitic cast iron with spheroidal graphite. DFG Project 504974025. Aachen.
[33] Thermo-Calc. (2023). TCFE9, TCS Steel/Fe -Alloys Database, Version 3.0.
[34] Thermo-Calc. (2023). MOBFE4, TCS Steel/FE Alloys Mobility Database version 4.
[35] Turnbull, D. (1953). Theory of catalysis of nucleation by surface patches. *Acta Metallurgica.* 1(1), 1953, 8-14. https://doi.org/10.1016/0001-6160(53)90004-2.
[36] Nellissery Rajan, R. (2024). *Experiment-based 3-D phase field simulations of nucleation and growth of graphite nodules in SGI alloys and evaluation of homogenized mechanical properties*. Master-Thesis. RWTH, Aachen.
[37] Eiken, J., Böttger, B. & Apel, M. (2023). Diffuse modelling of pearlite growth in Calphad-coupled multicomponent multi-phase-field simulations. *IOP Conference Series: Materials Science and Engineering.* 1281(1), 012051. DOI:10.1088/1757-899x/1281/1/012051.
[38] Fredriksson, H. & Svensson, I.L. (1984). Computer simulation of the structure formed during solidification of cast iron. *MRS Proceedings*. 34, 273. DOI: 10.1557/PROC-34-273.
[39] Lekakh, S.N., Zhang, X., Tucker, W., Lee, H.K., Selly, T. & Schiffbauer, J.D. (2020). Micro-CT quantitative evaluation of graphite nodules in SGI. *International Journal of Metalcasting.* 14(2), 318-327. DOI:10.1007/s40962-019-00354-9.

[40] Access e.V. (2024). HOMAT version 6.004.
[41] Bonora, N., & Ruggiero, A. (2005). Micromechanical modeling of ductile cast iron incorporating damage. Part I: Ferritic ductile cast iron. *International Journal of Solids and Structures*. 42(5), 1401-1424. DOI: https://doi.org/10.1016/j.ijsolstr.2004.07.025.
[42] Kosteski, L., Iturrioz, I., Batista, R.G. & Cisilino, A.P. (2011). The truss-like discrete element method in fracture and damage mechanics. *Engineering Computations (Swansea, Wales).* 28(6), 765-787. DOI:10.1108/02644401111154664.